Effects of charging rates on heat and gas generation in lithium-ion battery thermal runaway triggered by high temperature coupled with overcharge

Qianzhen Guo [a], Shaoyan Liu [b], Jiabo Zhang [a,*], Zhen Huang [a,c], Dong Han [a,c,**]

[a] *Key Laboratory for Power Machinery and Engineering, Ministry of Education, Shanghai Jiao Tong University, Shanghai, 200240, China*
[b] *China-UK Low Carbon College, Shanghai Jiao Tong University, Shanghai, 200240, China*
[c] *Shanghai Non-carbon Energy Conversion and Utilization Institute, Shanghai, 200240, China*

HIGHLIGHTS

- TR characteristics at thermal-electrical abusive conditions are revealed.
- The effects of charging rates on heat and gas generation are investigated.
- The promoted impacts of irreversible heat on TR is clarified.
- The nonlinear relationship between heat release and gas generation is elucidated.

ARTICLE INFO

ABSTRACT

Lithium-ion batteries are susceptible to thermal runaway incidents at high-temperature abuse and overcharging conditions. This study employs an experimental approach that combines an accelerating rate calorimetry with a battery testing system to investigate thermal runaway behaviors in 18,650-type $LiNi_{1/3}Co_{1/3}Mn_{1/3}O_2$ cells at high temperatures, particularly during constant current constant voltage (CCCV) charging at rates of 0.2C, 0.5C, 1C, and 2C. The results reveal that cells coupled with charging behavior exhibit a greater potential for thermal runaway at high temperatures, and increased charging rates lead to increased irreversible heat and promoted side reactions, which ensure advanced thermal runaway events and enhanced heat and gas generation capacity in the cell. Furthermore, owing to the combined influences of stage of charge and the promoting effect of charging current on side reactions, the total heat and gas production and the charging rate exhibit a nonlinear relationship. Eventually, after the completion of charging, the relationship between gas generation rate and heat generation rate can be characterized by two linear growth stages. The initial stage displays consistent gas generation rates despite variations in charging rates, and the subsequent stage demonstrates different gas generation rates with increased charging rates, suggesting alterations in side reaction pathways.

1. Introduction

Lithium-ion batteries (LIBs), characterized by high energy density, excellent cycling performance, and low self-discharge rate, have been widely applied in various fields such as portable devices, electric vehicles, and energy storage systems [1–3]. However, LIBs also face safety issues, especially for $LiNi_{1/3}Co_{1/3}Mn_{1/3}O_2$ (NCM) cells with higher energy density [4]. For instance, fire hazards and explosions can arise at abusive conditions, such as mechanical crashes [5,6], internal short circuits [7,8], overcharge [9–15], high-temperature abuse [16–18], and

so on. A great amount of heat and combustible gases are released simultaneously, characterized as thermal runaway (TR), which significantly constrains the development of LIBs.

Thermal abuse is the most widely cause of TR in LIBs. During the self-heating process, complex chain reactions occur among the active materials, including the cathode, anode, and electrolyte of LIBs [19,20]. Employing accelerating rate calorimetry (ARC), the characteristics of such reactions, such as the onset temperature, peak temperature, and heat generation rate can be obtained [21–24]. Besides thermal abuse, LIBs are also susceptible to TR triggered by electrical abuse. For instance, nearly 30% of TR incidents in electric vehicles are caused by

---

Nomenclature

LIB	lithium-ion battery
TR	thermal runaway
CC	constant current
CV	constant voltage
ARC	accelerating rate calorimetry
NCM	$LiNi_{1/3}Co_{1/3}Mn_{1/3}O_2$
LFP	$LiFePO_4$
LMO	$LiMn_2O_4$
SOC	state of charge
SOC_{fin}	final state of charge
BTS	battery testing system
GC	gas chromatography
DEC	diethyl carbonate
EMC	ethyl methyl carbonate
EC	ethylene carbonate
PVDF	polyvinylidene fluoride
OCV	open-circuit voltage
Δt_{CC}	the duration of CC charging (s)
Δt_{CV}	the duration of CV charging (s)
Δt_1	the duration of Stage I (s)
Δt_2	the duration of Stage II (s)
$\dot{Q}_{rev}$	reversible heat generation rate (W)
$\dot{Q}_{irrev}$	irreversible heat generation rate (W)
$\dot{Q}_{total}$	total heat generation rate (W)
$\dot{Q}_{side}$	the heat generation rate caused by side reactions (W)
$\dot{Q}_s$	the heat generation rate caused by internal short circuits (W)
I	charge current (A)
ΔV	voltage drop (V)
R	internal resistance (Ω)
τ_d	thermal runaway delay time (s)
T	cell temperature (°C)
T_0	the initial cell temperature (°C)
T_1	the onset temperature of self-heating (°C)
T_2	the final temperature of charging (°C)
T_3	the separator collapsing temperature (°C)
T_4	the maximum temperature of TR (°C)
P	the pressure in the jar (MPa)
P_0	the initial pressure in the jar (MPa)
P_1	the pressure of the cells at T_1 (MPa)
P_2	the pressure of the cells at T_2 (MPa)
P_3	the pressure of the cells at T_3 (MPa)
P_4	the maximum pressure of TR (MPa)
M_{cell}	cell weight (g)
C_p	specific heat capacity (J kg^{-1} K^{-1})
κ	the enhancement factor of heat generation rate of side reactions
n_g	the gas generation amount (mol)
Z_g	the compressible factor of generated gas
Z_0	the compressible factor of the initial gas
R_g	gas constant
V_a	the actual volume of the gas (m^3)
V_{jar}	the inner volume of the jar (m^3)
V_{LIB}	the volume of the cell (m^3)
V_{void}	the void space within the cell (m^3)
n_{sc}	the gas generation amount at T_3 (mol)
n_{max}	the total gas generation amount (mol)

the heat accumulation resulting from improper fast-charging practices [25]. Therefore, it is necessary to analyze the heat generation of LIBs undergoing TR resulting from electrical abuse [9–15,26–28]. Wang et al. [13] conducted a comparative analysis of overcharge behaviors and TR features in large format LIBs with varied cathode materials. Their findings indicated that for NCM cells, the heat generation caused by charging behavior contributed to about 21.5% of the heat accumulation leading to TR events, whereas for LiFePO$_4$ (LFP) cells, this percentage was measured to be 39.4%. Liu et al. [14] similarly conducted heat generation analyses of TR in LiMn$_2$O$_4$ (LMO) cells induced by overcharging. They further pointed out that irreversible heat and reversible heat are the primary sources of initial heat accumulation, while subsequent reactions between plated lithium and electrolyte generate a substantial amount of heat. These exothermic reactions are the key factor for overcharge-induced TR.

In practical applications, TR can be triggered due to several abusive forms, such as a combination of thermal abuse and electrical abuse [29–33]. Some studies have as such examined the effects of environmental temperature [29,33], heating power [30], current magnitude [29–33], and other factors on the thermal behavior of LIBs at thermal-electrical coupling conditions. For example, Hu et al. [32] discovered that with the increase in charging rate from 1C to 5C, the average triggering temperature of TR is reduced by 30.3 °C, and the ratio of heat generated during cell charging to the overall heat accumulation prior to TR is elevated from 2.0% to 28.1%. The substantial amount of plated lithium in the negative electrode with a high State of Charge (SOC) and the heat generated during charging were deemed responsible for the enhanced risk of TR. Meng et al. [33] pointed out that LIBs charging with a high charging rate at elevated ambient temperatures exhibited a higher potential for thermal risk. As the ambient temperature rises from 2 °C to 56 °C, the occurrence of venting events and

violent TR events is advanced by 115–143s, but the total heat production will be reduced due to the shortened charging duration. Conversely, the proportion of charging heat increased from 1% to 9% as the charging rate elevated from 0.5C to 3C. The aforementioned study found that the existence of charging behavior promotes the heat accumulation before severe TR occurs. However, the mechanisms through which charging behavior affects the side reactions remain unclear and warrant investigation.

Analyzing gas generation characteristics helps understand the kinetics of side reactions. Additionally, the combustible gases produced by side reactions determine the combustion and explosion of LIBs after TR [34–36]. To this end, it is necessary to analyze the gas generation and internal pressure evolution of LIBs. To obtain pressure data inside LIB, Schmitt et al. [37] designed a prismatic NCM cell equipped with pressure sensors. During battery operation, a nonlinear relationship between internal gas pressure and temperature is observed due to the evaporation of electrolytes. Furthermore, Qin et al. [38] removed the top cap of a commercial 18,650-type NCM cell and placed it in an airtight jar for ARC tests. The results indicated that during the self-heating phase, the generated gases originated from both electrolyte evaporation and side reactions. They pointed out that the relationship between temperature and gas generated from side reactions is approximately linear when the temperature approaches the triggering point of TR event. Subsequently, Jia et al. [39] employed a similar methodology to analyze gas evolution during the TR processes of LFP, LMO, and NCM cells. The results indicated that the relationship between the rate of temperature rise and the rate of gas generation is different for cells with various cathode materials. It is evident that acquiring internal pressure data through airtight jar and capless cells is an effective approach to investigate the gas generation behavior of LIBs at high-temperature abuse conditions. However, currently, this method is not applied for studying the gas

generation behavior of cells subjected to the charging process.

The primary purpose of this study is twofold: 1) to calculate the heat generated due to the charging behavior and clarify the influence of charging on the side reactions caused by high temperature, and 2) to analyze the gas production behavior and its relationship with side chemical reactions during TR. Specifically, ARC was combined with a Battery Testing System (BTS) to establish an experimental platform for investigating the TR behavior resulting from thermal-electrical coupling abuse in LIBs. In the tests, the commercially 18,650 NCM LIBs with opened top caps were placed in an airtight jar and charged with the constant current constant voltage (CC-CV) charging method at 90 °C. The CC charging rates applied were 0.2C, 0.5C, 1C, and 2C, and the voltage during the CV charging phase remained at 5V. Through a pressure sensor connected to the airtight jar, pressure data were collected, and the composition of gases generated during TR was obtained using Gas Chromatography (GC). This enabled a comprehensive analysis of the heat and gas generation behaviors throughout the TR process. These findings are instrumental in illuminating the mechanisms underlying TR induced by charging in high-temperature environments, and have implications for the safety and performance optimization of LIBs in various applications.

2. Experimental setup and methods

2.1. Battery samples and processing

The sample cells used in this study were commercial 18,650 NCM LIBs (Shenzhen Doublepow Technology Co., Ltd., China), and their basic parameters are listed in Table 1. To determine the exact capacity of the cells, five charge and discharge cycles with the CC-CV charging method were conducted on the cell using a BTS (CT-4008-5V20A-A, Shenzhen Neware Technology Co., Ltd., China). Specifically, the cells were charged at 0.5C until reaching the cut-off voltage of 4.2V, following which they were charged at a constant voltage until the current decayed to the cut-off current of 0.04A. Following a waiting period of 30 min, the cells were discharged at 0.5C until they reached the cut-off voltage of 2.5V. After five cycles, the average measured cell capacity was taken as the actual capacity.

To obtain the internal pressure evolution during the self-heating process, the top cap of the cell was opened in a nitrogen-filled glove box, and this procedure did not affect the chemical properties of the cell [39,40]. Subsequently, two wires were soldered onto the positive and negative terminals to guarantee the feasibility of the connection between the cell and the BTS. It should be noted that when unsealing the top cap, the structural integrity of the anode nickel tab should be ensured, as it directly influences the charging and discharging capability of the cell.

2.2. Experimental setup

As shown in Fig. 1, the airtight jar containing the pre-treated test sample was placed inside the ARC (BAC-90A, Hangzhou YOUNG Instruction Science & Technology Co., Ltd., China), and the jar has an inner radius of 39 mm and a height of 68 mm. To ensure the uniform distribution of cell temperature, two N-type thermocouples were affixed to the middle of the surface of each cell. Besides, the wires connecting to the terminals of the cell were threaded through pre-existing holes in the airtight jar to achieve cell charging during the ARC test. Subsequently, these wires were linked to the BTS, which enabled the acquisition of voltage and current data. To acquire pressure data, a gas circuit was affixed to the airtight jar, with the opposite end of the gas circuit being attached to a pressure sensor sampling at a high frequency of 100 Hz. Following the occurrence of a violent TR event, the valve within the gas circuit was opened, enabling the generated gases to be introduced into a GC (Agilent 7890B) for compositional analysis. Note that the interior of the airtight jar underwent backflushing using nitrogen to establish an inert gas environment, and the integrity of the sealing was also confirmed.

Prior to carrying out the TR experiments involving charging behavior, a set of control experiments at exclusively thermal abuse conditions were conducted. In these experiments, the cells with 70% SOC were employed. This choice is made to ensure a requisite quantity of active material within the cell to induce conspicuous and repeatable TR, while also guaranteeing an adequate charging duration with the CC-CV charging method. Note that, the cells were allowed to rest at room temperature for 24 h after charging completion to maintain the stability of their electrochemical state. During this experiment, the heat-wait-seek mode of the ARC was employed, with an initial temperature of 55 °C, an increasing temperature step of 5 °C, and a temperature sensitivity of 0.01 °C·min^{-1}. The temperature at which the self-heating rate exceeded 0.01 °C·min^{-1} was considered as the onset temperature of self-heating (T_1) [24,38,39], which was detected to be 90 °C.

In the experiments involving high-temperature coupled with charging behavior, the initial temperature for charging was set at 90 °C, consistent with T_1 observed in the thermal abuse experiment. Specifically, after placing the airtight jar into the ARC, a constant temperature heating mode at 90 °C was applied. Until the cell reached 90 °C, the BTS was initiated for charging. To better reflect the practical usage scenarios, the CC-CV charging method was employed. The charging rates at the CC charging phase employed were 0.2C, 0.5C, 1C, and 2C, while the subsequent CV charging phase maintained a voltage of 5V, which is higher than 4.2V to confirm the overcharge conditions. Simultaneously with the start of charging, the cell was subjected to adiabatic conditions until reaching the peak temperature of TR. Subsequently, the valve was opened to channel the generated gases into the GC for compositional analysis. According to the charging rates during the CC charging phase, these series of experiments were labeled as 0.2C Test, 0.5C Test, 1C Test, and 2C Test, and the thermal abuse experiment conducted without charging was identified as the 0C–70%SOC Test. In this study, each test was repeated at least twice to ensure reproducibility of the key parameters, and the observed differences in results have negligible impact on the overarching trends, thereby not compromising the validity of our conclusions.

2.3. Measurement of heat source caused by charging

The heat generation during the charging process of LIBs can be divided into reversible heat Q_{rev} and irreversible heat Q_{irrev}, where reversible heat is caused by the entropy change in the charging and discharging process of the cells, and it can be expressed as follows [51, 52]:

$$\dot{Q}_{rev} = -IT\frac{\partial U_{OCV}}{\partial T} \tag{1}$$

where $\dot{Q}_{rev}$ is the reversible heat generation rate, T is the cell temperature, I is the charge current, and U_{OCV} represents the open-circuit voltage (OCV). The entropic heat coefficient, $\partial U_{OCV}/\partial T$, can be obtained by measuring the OCV changes of the cell with different SOCs at various
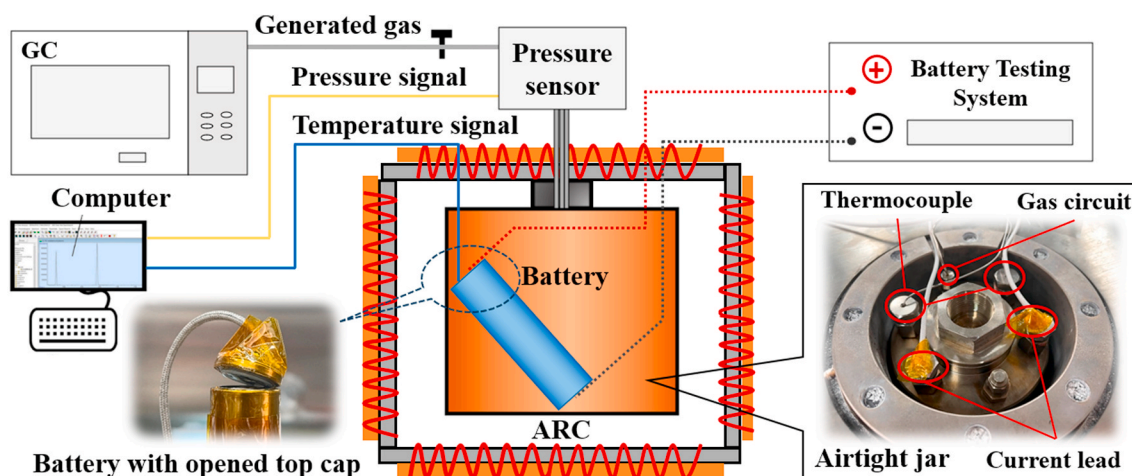
Table 1
Summary of the sample LIB specification.

Item	Specification
Dimensions (mm)	18 (diameter) × 65 (height)
Naked cell weight (g)	41.63 ± 0.10
Specific heat capacity (J·kg^{-1}·K^{-1})	944.80
Cathode material	LiNi$_{1/3}$Co$_{1/3}$Mn$_{1/3}$O$_2$
Anode material	Graphite
Electrolyte solvents	DEC: EMC: EC
Salt	LiPF$_6$
Rated capacity (Ah)	2.54 ± 0.02
Nominal voltage (V)	3.70 ± 0.05

Fig. 1. Schematic of the experimental setup for temperature, current, voltage, pressure, and generated gas measurement during the TR of LIBs.

temperatures [52–54]. Specifically, the cell with a given SOC of 70% was maintained for 4h at temperatures of 20, 40, and 60 °C to measure the entropic heat coefficient. To obtain the relationship between the entropy heat coefficient and SOC, the cell was charged to 80%, 90%, and 100% SOC, and the previous test was repeated for each SOC. Note that a 24-h relaxation time should be guaranteed after each charge.

Irreversible heat includes ohmic heat and polarization heat, which are caused by current passing through ohmic resistance and cell polarization, respectively [51,55]. The intermittent current method is an effective approach to quantifying irreversible heat [10,53,56]. Therefore, 0.2C–2C charging tests were repeated using the intermittent current method with an interval of 60s. The voltage drop ΔV between two charging intervals is considered to be attributed to the ohmic resistance and cell polarization together [55]. The internal resistance R and irreversible heat generation rate $\dot{Q}_{\mathrm{irrev}}$ of the cell can be obtained by Eqs. (2) and (3).

$$R = \frac{\Delta V}{I} \tag{2}$$

$$\dot{Q}_{\mathrm{irrev}} = I^2 R \tag{3}$$

3. Results and discussion

3.1. Overall TR behaviors for cells with different charging procedures

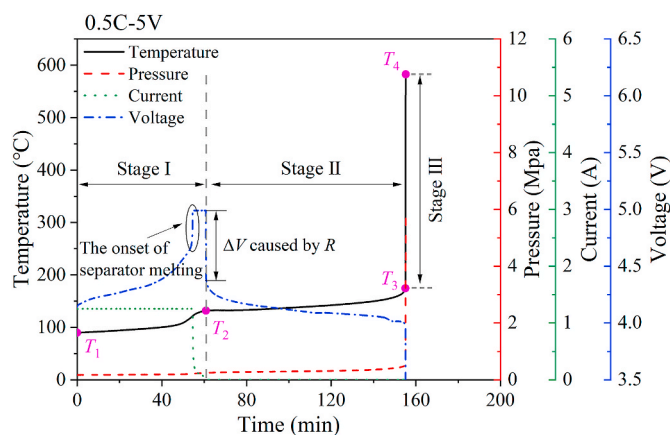The temperature, pressure, current, and voltage curves of the cell at

0.5C Test are depicted in Fig. 2 as an example to explore the TR characteristics. Four key thermal characteristic temperatures $\{T_1, T_2, T_3, T_4\}$ are observed to describe the TR process. Specifically, T_1 is the onset temperature of the self-heating, T_2 is the final temperature of charging, T_3 is the separator collapsing temperature, and T_4 is the maximum temperature of TR. Note that T_3 is defined as the temperature when the temperature rise rate exceeds $1\ °\mathrm{C}\cdot\mathrm{s}^{-1}$ [24]. Moreover, based on these characteristic temperatures, the progression from the initiation of self-heating to the peak temperature of TR is divided into three stages {Stage I, Stage II, Stage III}. Based on the data obtained from BTS, it was observed that the final state of charge (SOC$_{\mathrm{fin}}$) at the end of CC-CV charging process in the 0.2C–2C Tests did not exceed 120%. To distinguish the respective contributions of charging behavior and total energy of the cell to TR, a comparative analysis was conducted using a set of thermal abuse experimental data for the cell with 120% SOC from our previous study [45]. The characteristic temperatures of all six tests, along with the durations of the initial two stages $\{\Delta t_1, \Delta t_2\}$, are summarized in Table 2.

Stage I refers to the period from T_1 to T_2, during which the cell undergoes CC-CV charging until it reaches a cut-off current of 0.04A. In contrast to overcharge experiments initiated at room temperature [57, 58], the present study demonstrates that the cell terminal voltage undergoes an abrupt increase to 5V at the end of CC charging, as illustrated in Fig. 2, rather than exhibiting a gradual rise from the initial voltage. This phenomenon is attributed to the failure of the cell separator at high temperatures [59,60]. The melting of the separator leads to micro-short circuits (MSC) within the cell, which causes an increase in the cell internal resistance [60–62], thereby resulting in an abrupt rise in the terminal voltage. With the continuous failure of the separator, the charging current experiences a swift decline during the subsequent CV charging phase. At the shutdown temperature of the separator, typically 135 °C, the charging current diminishes to the cut-off value of 0.04A, causing an instantaneous drop in the cell terminal voltage due to the

Fig. 2. The variations in temperature, pressure, current, and voltage during TR process in the cell coupled with 0.5C charging.

Table 2
TR features for the cells.

	T_1/ °C	Δt_1/ s	T_2/ °C	Δt_2/ s	T_3/ °C	T_4/ °C	SOC$_{\mathrm{fin}}$
0C–70%SOC Test	90.0	–	–	–	201.7	367.9	70%
0.2C Test	90.0	9263	137.5	3202	182.7	866.2	118.7%
0.5C Test	89.9	3651	131.7	5655	174.7	582.7	114.9%
1.0C Test	89.9	2279	126.3	4222	174.1	511.3	110.0%
2.0C Test	90.1	4385	137.8	2519	187.6	642.8	102.5%
0C–120%SOC Test	90.5	–	–	–	167.4	451.1	120%

substantial internal resistance. In stage II, because of the continuous discharge caused by MSC, the cell terminal voltage experiences a steady decline until the end of stage II [62,63]. Moreover, it is observed that during Stage I and Stage II, the pressure curve experiences a smooth increase before the temperature reaches T_3. This is because, during these two stages, the cell gradually releases heat while also producing a small amount of gas [38,39].

When the temperature of the cell reaches T_3, the complete failure of the separator results in a severe internal short circuit, which causes the terminal voltage to instantaneously drop to zero, leading the cell into an intense heat generation stage, namely Stage III. During this stage, a substantial amount of heat is generated due to the internal short circuit within the cell. Concurrently, the cell undergoes violent side reactions, including reactions between electrode materials and the electrolyte, electrolyte decomposition reactions, polyvinylidene fluoride (PVDF) decomposition reactions, and so on [24,41–43]. Simultaneously with the release of a substantial amount of heat, a significant quantity of gas is generated. This phenomenon results in a sharp increase in both the temperature and pressure curves during Stage III, eventually reaching their peak values.

As plotted in Fig. 3, the temperature and pressure evolution curves among the six cells were compared, where P_1, P_2, P_3 correspond to the pressure of the cells at T_1, T_2, T_3, respectively, while P_4 represents the maximum pressure of TR. It is observed that charging behavior significantly affects the TR process of the cells. First, the charging behavior significantly accelerates the occurrence of TR events. As shown in Fig. 3, the non-charging cell takes approximately 800 min to reach T_3 (delay time for TR, τ_d) while τ_d is reduced to a range of 108–206 min for cells coupling with the charging behavior, which is roughly 1/8 to 1/4 of the τ_d observed in 0C–70%SOC Test and 0C–120%SOC Test. Second, $T_3 = 201.7$ °C and $P_3 = 0.62$ MPa in 0C–70%SOC Test exceeded those of 0.2C–2C Tests with $T_3 \in [174.1, 187.6]$ °C, $P_3 \in [0.51, 0.52]$ MPa. This indicates that, at conditions involving charging behavior, the cell exhibits a higher risk of TR. However, this phenomenon is primarily attributed to the increase in cell SOC_{fin} caused by charging, as their T_3 and P_3 values did not exhibit lower levels compared to $T_3 = 167.4$ °C and $P_3 = 0.50$ MPa in the 0C–120%SOC Test. Third, the presence of charging behavior also significantly raises T_4 and P_4, which suggests that charging behavior can enhance the TR hazards of the cell. It should be noted that this promoting effect cannot be solely attributed to the increase in SOC_{fin}. Even when compared with the results from the 0C–120%SOC Test, the T_4 and P_4 values in the 0.2C–2C Tests remained significantly higher, despite having a lower SOC_{fin} than 120%.

By the comparison of the four cells coupled with charging behavior as plotted in Fig. 3, several points can be made. First, it is observed that,

as the charging rate during the CC charging phase increases from 0.2C to 1C, T_3 decreases from 182.7 °C to 174.1 °C. Conversely, in the 2C Test, due to the shortened duration of the CC charging phase, an extended period of low current is experienced, resulting in a higher T_3 compared to 0.2C–1.0C Tests. Second, P_3 in 0.2C–2C Tests is all close to 0.51 MPa, indicating that the influence of varying charging rates on P_3 can be neglected. Finally, the relationship between T_4 and P_4 and the SOC_{fin} is nonlinear. This may be attributed to the influence of side reactions caused by the operating current, resulting in changes to their heat generation and gas production characteristics. A detailed analysis will be carried out later.

To further analyze the exothermic process during the TR of LIBs, Fig. 4 presents the temperature rise rate, dT/dt, of the cells as a function of their temperature. Additionally, the three stages, from the onset of self-heating reaction to the peak temperature, have been highlighted. For the cells coupled with charging behavior, their dT/dt is notably higher than that of the cells without charging. Specifically, at the onset of charging, the dT/dt experiences a rapid rise due to the heat generation caused by charging behavior, and an increased charging current leads to an intensified dT/dt. During the CC charging phase, the dT/dt increases with the elevation of the temperature, and the magnitude of dT/dt depends on the charging rate and the duration of CC charging. Subsequently, as the charging method switches from CC to CV, the continuously diminishing charging current leads to a negative
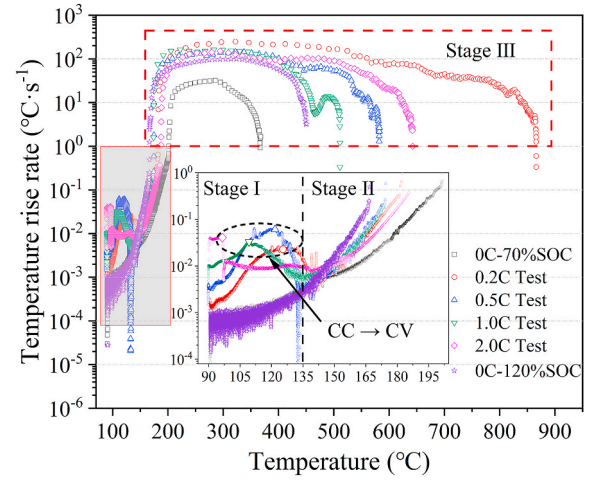

Fig. 4. Temperature rise rate as a function of temperature of six cells.
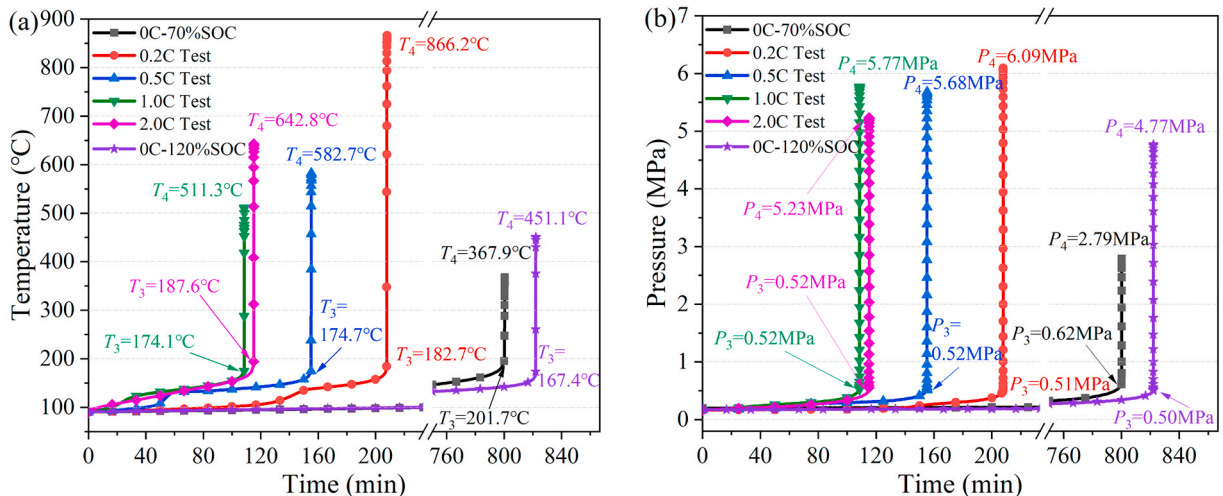

Fig. 3. The comparison of TR behavior among cells with different charging procedures and the cell without charge: (a) temperature evolution, (b) pressure evolution.

relationship between dT/dt and temperature. Following the completion of CC-CV charging process, the heat generation enters Stage II, and the heat generation caused by charging behavior no longer contributes to heat accumulation, while exothermic side reactions persist. Therefore, the dT/dt in Stage II continues to steadily rise until the cell enters Stage III of the TR process. Moreover, for the cells without charging behavior, there was no significant difference in the dT/dt curve between 70% SOC cell and 120% SOC cell before the failure of the separator. This indicates that it was indeed the charging behavior that significantly enhanced heat generation during stage I, rather than the SOC$_{fin}$. In Stage II, the 120% SOC cell exhibits the highest temperature rise rate, indicating that SOC$_{fin}$ plays a dominant role in the heat generation of the cell during this stage. However, in Stage III, both the maximum temperature and the peak temperature rise rate of the 120% SOC cell are lower than the other four tests coupled with charging, despite reaching a SOC$_{fin}$ lower than 120% at the end of the CC-CV charging process. This suggests that cells subjected to combined high-temperature and charging conditions demonstrate greater explosion hazard compared to cells subjected to sole thermal abuse, and this is attributed to the charging behavior in stage I.

3.2. The heat generation analysis for cells with different charging procedures

As mentioned above, the heat accumulation during Stages I primarily consists of reversible heat Q_{rev}, irreversible heat Q_{irrev}, and heat generated by side reactions Q_{side}, while other heat contributions such as mixing heat and phase transition heat are neglected due to their insignificance [44]. Following the end of Stage II, the collapse of the separator inside the cells results in a massive internal short circuit, thereby

the cells releasing a substantial amount of heat, Q_s [13]. This is accompanied by the release of a significant amount of heat generated by side reactions. Note that, the cell is assumed to be in an adiabatic environment, and the heat generation rates for each stage can be calculated using Eq. (4).

$$\dot{Q}_{total} = M_{cell}C_p\frac{dT}{dt} = \begin{cases} \dot{Q}_{side} + \dot{Q}_{irrev} + \dot{Q}_{rev}, \text{Stage } I \\ \dot{Q}_{side}, \text{Stage } II \\ \dot{Q}_{side} + \dot{Q}_s, \text{Stage } III \end{cases} \quad (4)$$

where M_{cell} is the cell weight, C_p is the specific heat capacity of the cell, $\dot{Q}_{total}$ denotes the total heat generation rate of the cell, $\dot{Q}_{side}$ denotes the heat generation rate caused by side reactions, and $\dot{Q}_s$ represents the heat generation rate caused by internal short circuits.

The presence of charging behavior has a significant impact on the heat generation in stage I. In addition to the enhanced heat release resulting from side reactions, the irreversible heat of the cell is substantially increased, because of the elevated internal resistance from separator melting, causing the reversible heat to be significantly lower in magnitude. Through the measurement of the entropy heat coefficient, it was observed that even during the initial stage of charging before any influence on the internal resistance, the magnitude of reversible heat remained considerably lower than that of irreversible heat. Therefore, reversible heat is neglected in the analysis of heat generation of the cells.

As illustrated in Fig. 5, the variations in current and internal resistance are depicted, and both the irreversible heat generation rate and the side reaction heat generation rate are quantified. It is observed that the heat generated by side reactions remains the primary source of heat in stage I and exhibits a correlation with separator failure, similar to that of irreversible heat. However, it can also be noted that except for the
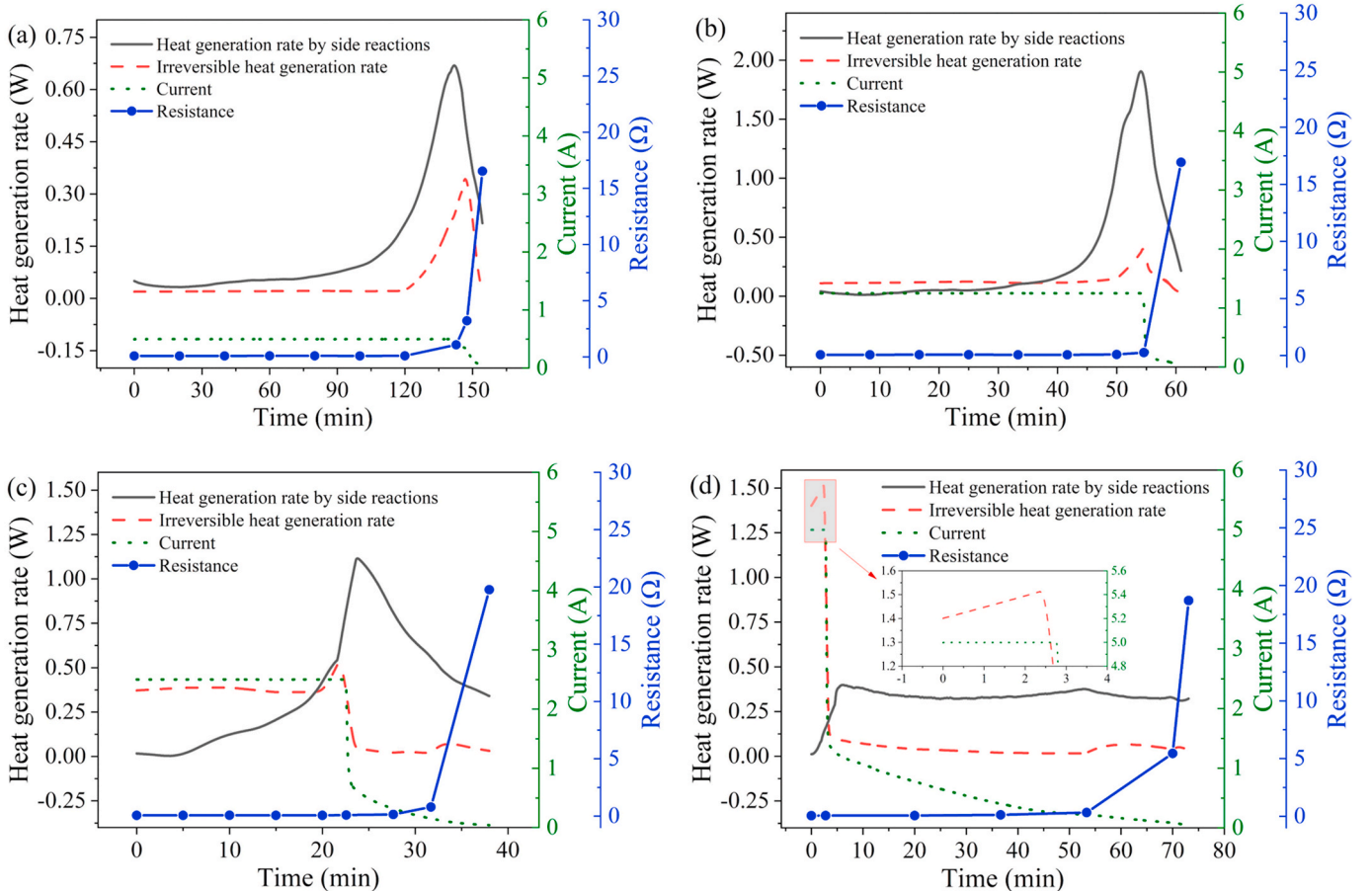

Fig. 5. The heat generation rate, current, and resistance during CC-CV charging process: (a) 0.2C Test; (b) 0.5C Test; (c) 1.0C Test; (d) 2.0C Test.

0.2C Test, during the early stage of heat accumulation, the rate of irreversible heat generation exceeds that of side reaction heat generation. Furthermore, as the charging rate increases, the dominance of irreversible heat in early-stage heat accumulation becomes more prominent. For cells subjected to solely thermal abuse conditions, within the temperature range of stage I, their heat generation rate remains relatively low for an extended duration, as shown in Fig. 4. This necessitates a significant amount of time for the cells to trigger TR. In contrast, the cells influenced by charging can rapidly complete stage I, leading to a substantial reduction in the delay time for TR.

As mentioned earlier, the maximum temperature in 0.2C–2C Tests, which represents the total heat generation during the overall TR process, exhibits a nonlinear relationship with SOC_{fin} and charging rate. In the 2C Test, a greater heat generation is observed despite having a lower SOC_{fin} when compared to the 0.5C and 1C Tests. This phenomenon can be attributed to the enhancing effect of the prolonged current on side reactions.

To further analyze the promoting effect of current on the heat generation rate of side reactions, Fig. 6 illustrates the κ value, which is calculated by Eq. (5) and quantifies the promoting effect of charging behavior on the heat generation rate of side reactions:

$$\kappa = \frac{\dot{Q}_{side,i\ C\ Test}}{\dot{Q}_{side,0C-70\%SOC\ Test}}, i = 0.2, 0.5, 1.0, 2.0 \tag{5}$$

The results reveal that during the CC charging phase, an increased κ is achieved with elevated temperature. Besides, κ gradually decreases after the charging method transitions, correlating with the diminishing current, ultimately approaching 1. This is reasonable since, at CV charging conditions, the charging current gradually diminishes, leading to a reduced impact on side reactions. Additionally, it can be observed that with an increase in the charging rate during the CC charging phase, the promoting effect of charging behavior on the heat release from side reactions is enhanced. This results in a significantly higher κ value of the 2.0C test in the CC charging phase compared to the other three test cases. As documented in Ref. [45], within the temperature range characterizing Stage I, there is no significant difference in the heat release rate between 70% and 120% SOC. Therefore, the influence of the SOC can be neglected. Among 0.2C–2C Tests, the 0.5C Test exhibits the highest peak κ value, reaching 40, followed by $\kappa = 30$ in the 1C Test, $\kappa = 15$ in the 2C Test, and $\kappa = 13$ in the 0.2C Test. This is determined by the positive relationship between the charging rate and cell temperature on κ. For instance, the 0.2C Test reaches the highest temperature when the charging method transitions but has the lowest charging rate, while the

2C Test has the highest charging rate but the lowest temperature when the charging method transitions, resulting in lower κ values for both.

3.3. Gas generation analysis for cells with different charging procedures

During the TR process of LIBs, not only a significant amount of heat is generated, but also a considerable amount of combustible gas is released. To investigate the characteristics of gas generation, it is necessary to determine the produced gas quantity, denoted as n_g, and it can be calculated using the ideal gas state equation [38,39,46], as shown in Eq. (6).

$$n_g = \frac{V_a P}{Z_g R_g T} - \frac{V_a P_0}{Z_0 R_g T_0} \tag{6}$$

where P and P_0 are the actual and initial pressure in the jar, T and T_0 are the actual and initial temperature of the cell, Z_g and Z_0 are the compressible factors of the generated gases and initial gases, and can be set as 1 [38,39,47,48]. R_g is the gas constant of 8.314 J mol^{-1} K^{-1}, V_a is the actual volume of the gas and can be calculated by Eqs. (7) and (8) [38]:

$$V_a = V_{jar} - V_{LIB} + V_{void} \tag{7}$$

$$V_{void} = 0.07 V_{LIB} \tag{8}$$

where V_{jar} denotes the inner volume of the jar of 3.25×10^{-4} m^3, V_{LIB} denotes the volume of the cell of 1.65×10^{-5} m^3, and V_{void} represents the void space within the test cell.

The variations in the gas generation quantity during the TR process of LIBs are depicted in Fig. 7, where n_{sc} represents the gas generation at T_3, and n_{max} stands for the final gas generation quantity. Note that the gas quantity includes products from both side reactions and electrolyte evaporation [37,49,50]. Additionally, due to the high local and temporal gradients within the jar during the violent TR event, it is necessary to wait until the gas reaches a thermodynamic equilibrium state to calculate n_{max} [48]. It is observed that the n_{max} for the 0.2C–1C Tests are 0.272 mol, 0.265 mol, and 0.268 mol, respectively, which are higher than those of the 0C–70%SOC Test and 0C–120%SOC Test. This indicates that charging behavior promotes the gas-generation capacity of cells in TR events, and this promoting effect is independent of the contribution of SOC.

Although there are variations in n_{max}, the n_{sc} distribution for the 0.2C–2C Tests falls within the range of [0.029, 0.031] mol, displaying only marginal differences among these cases. Moreover, compared to the observed n_{sc} of 0.036 mol in the 0C–70%SOC Test, the n_{sc} in 0.2C–2C
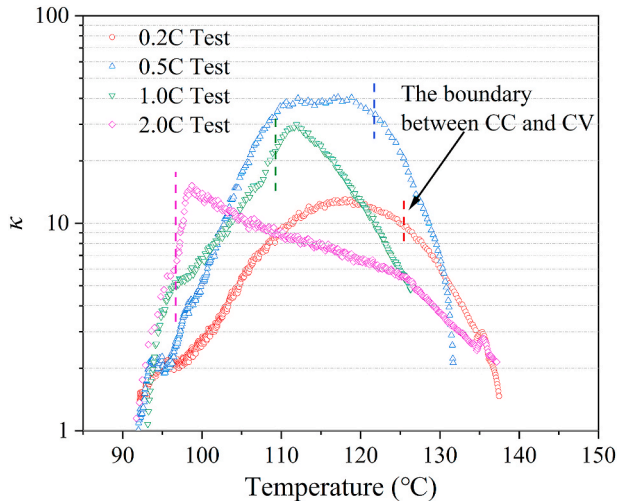

Fig. 6. The curves of κ as a function of temperature for the cells with different charging procedures.
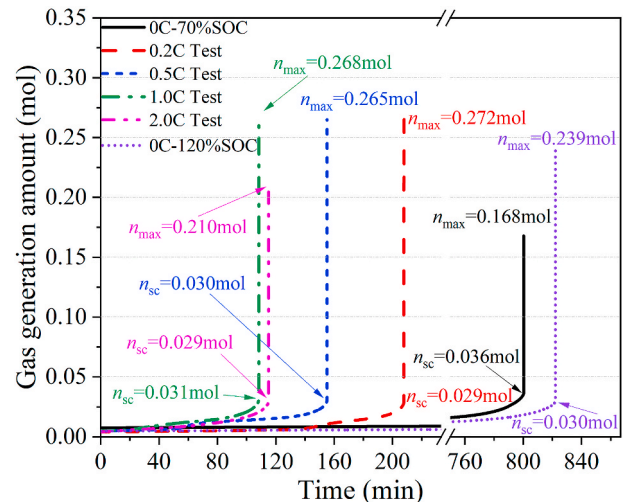

Fig. 7. The gas generation amount evolution of six cells.

Tests demonstrates a reduction ranging from 13.9% to 19.4%. However, there is no significant change compared to the n_{sc} of 0.030 mol in the 0C–120%SOC Test. This indicates that the enhanced risk of TR is primarily due to the increased total energy of the cells.

The variations in gas generation rate during the TR process are related to the side reaction process within the cells. As shown in Fig. 8a, the variations in gas generation rate with temperature for all cells were plotted. It is observed that, similar to the temperature rise rate curves in Fig. 4, the gas generation rates for the cells subjected to charging behavior are higher than those in the 0C–70%SOC Test and 0C–120% SOC Test. Due to the mode transition and the end of charging behavior, they exhibit a non-monotonic relationship between gas generation rate and temperature. Specifically, during the CC charging phase, the gas generation rate is largely proportional to the charging rate. However, during the CV phase, the gas generation rate must be considered in conjunction with both the charging current and the cell temperature. In Stage I, the 0.5C Test exhibits the highest peak gas generation rate. When the cell temperature exceeds 140 °C, the gas generation rates in all four tests monotonically increase with temperature elevation and are lower than the gas generation rate observed in the 0C–120%SOC Test. This finding suggests that the gas generation in stage II is dominated by the SOC of the cells.

To clarify the relationship between gas and heat generation, the variations of gas generation rate with heat generation rate are illustrated in Fig. 8b. It is observed that, following the end of the charging process, the relationship between gas generation rate and heat generation rate can be divided into two linear growth stages, which are highlighted in Fig. 8b. In the initial stage, the gas generation rates are nearly identical for cells with different charging rates. This indicates that during this stage, the side reaction mechanisms among the active materials within the cells remain unaffected, and only the reaction rate is accelerated. Upon surpassing a heat generation rate threshold of 1 J s^{-1}, the gas generation transitions to the second stage, characterized by a linear increasing curve with a diminished slope, and the differences become more pronounced. In particular, it is noticeable that the slope of curves in the 0.2C–2C Tests all exceed that of the 0C–70%SOC Test and may even surpass that of the 0C–120%SOC Test. Moreover, elevated charging rates result in larger linear increase slopes in the second stage. This observation implies that, during this stage, there has been an alteration in the side reaction pathway, and the increased current could augment the gas generation associated with these side reactions. When the charging rate in the CC charging phase exceeds 2C, the extended CV charging phase with decaying current results in a reduction in the overall operating current throughout the cycle of the cells, thereby weakening their gas generation capability.

Following the end of TR, the gas composition generated from the cells was analyzed using GC, and the results were summarized in Table 3. The results reveal that the major components of the generated gases include hydrogen (H_2), methane (CH_4), carbon monoxide (CO), and carbon dioxide (CO_2), collectively comprising approximately 90% of the detected gases. Additionally, trace amounts of combustible gases such as ethylene (C_2H_4) and ethane (C_2H_6) are present, while the initial presence of nitrogen (N_2) and combustible gases with molecular weights greater than C3 were neglected.

Compared to the results in the 0C–70%SOC Test and 0C–120%SOC Test, there is a significantly higher proportion of combustible gases, e.g. H_2, CH_4, and CO, in the generated gases. Conversely, the inert gas CO_2 accounts for less than 43%, notably lower than the high proportion of 64.8% observed in the 0C–70%SOC Test and 49.0% observed in the 0C–120%SOC Test. These observations indicate that cells coupled with charging exhibit a greater potential for TR hazards.

4. Conclusions

Employing an accelerating rate calorimeter and a battery testing system, this study investigated the TR behavior of 18,650-type LiNi$_{1/3}$Co$_{1/3}$Mn$_{1/3}$O$_2$ cells with various CC-CV charging procedures (0C–70% SOC Test: no charging, 0.2C Test: 0.2C–5V, 0.5C Test: 0.5C–5V, 1C Test: 1C–5V, 2C Test: 2C–5V, 0C–120%SOC Test: no charging) at an initial ambient temperature of 90 °C. Based on the observed four key thermal characteristic temperatures {T_1, T_2, T_3, T_4}, the processes from the onset of self-heating reactions to the peak temperature of TR were divided into three stages, denoted as Stages I to III. The evolution of the internal pressure was obtained through an airtight jar and a connected pressure sensor, and the effects of charging rate on the gas generation behavior of cells during TR were explored based on the ideal gas assumption. Moreover, the relationship between gas generation and heat release in the cells, as well as the composition of the generated gases, were

Table 3
Composition of generated gases.

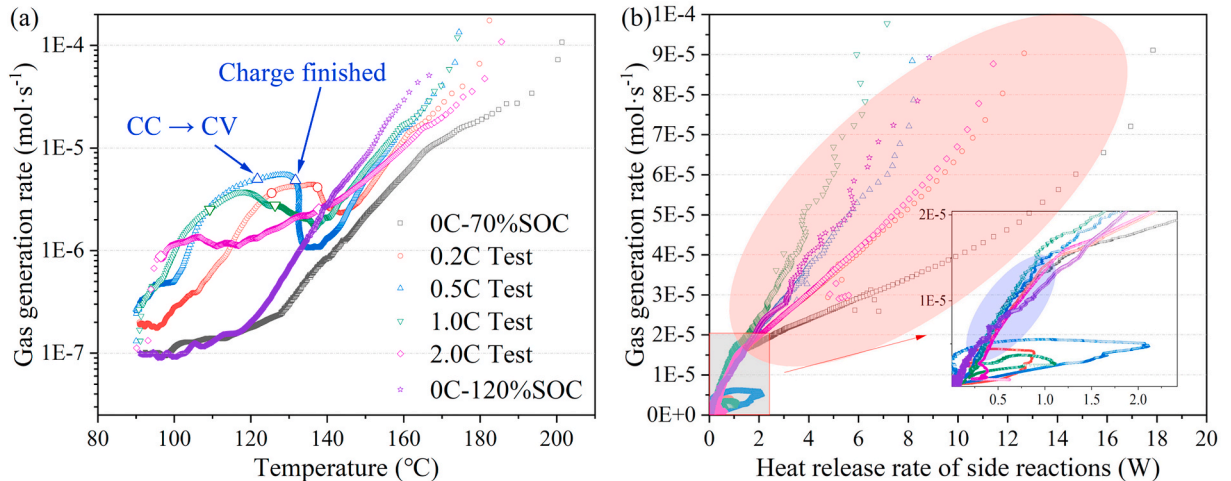|	0C–70% SOC Test	0.2C Test	0.5C Test	1C Test	2C Test	0C–120% SOC Test
H_2	15.7%	22.6%	21.4%	23.5%	20.0%	23.5%
CH_4	5.86%	11.3%	11.3%	10.3%	9.67%	9.12%
C_2H_4	0.86%	0.48%	0.44%	0.45%	0.94%	1.73%
C_2H_6	1.85%	2.16%	2.50%	2.25%	2.45%	2.14%
CO_2	69.1%	35.2%	38.9%	37.0%	42.6%	49.0%
CO	6.71%	28.4%	25.5%	26.5%	24.4%	14.5%

Fig. 8. The variations of gas generation rate with respect to (a) temperature (b) $\dot{Q}_{side}$ curves of six cells.

investigated. The main conclusions of this study are as follows.

(1) The cells subjected to combined high-temperature abuse and charging conditions exhibit an enhanced TR hazard, characterized by an increase in total heat and gas generation, as well as a significantly higher proportion of combustible gases such as H_2, CH_4, and CO. Additionally, these cells also exhibit a greater risk of TR, as indicated by lower critical temperature and gas production triggering TR.

(2) In Stage I, the elevated hazards of TR are primarily attributed to the irreversible heat generated during the charging process and the side reaction heat reinforced by the current. In Stage II, the heat and gas generation behavior of the cell is dominated by SOC, which is responsible for the enhanced risks of TR. Owing to the combined influences of SOC and the promoting effect of charging current on side reactions, a nonlinear relationship between total heat and gas production and the charging rate is achieved.

(3) The enhanced side reaction dominates the temperature rise in stage I, but when the charging rate is not lower than 0.5C, the irreversible heat generation rate exceeds the side reaction heat during the early stage of heat accumulation, serving as the primary reason for the premature triggering of TR. With an increased charging rate, the irreversible heat generation rate rises, and a more pronounced promoting effect on side reactions is achieved. Simultaneously, they exhibit a correlation between the increased internal resistance caused by separator failure.

(4) The relationship between the gas generation rate and heat generation rate of the cells after charging can be delineated into two linear growth stages. The first stage remains unaffected by the charging process, while the second stage, characterized by a reduced rate of curves, demonstrates a pronounced association with the charging. It is noteworthy that the rate of curves in the second stage becomes steeper as the magnitude of the charging current increases.

CRediT authorship contribution statement

Qianzhen Guo: Writing – original draft, Methodology, Investigation, Formal analysis, Data curation. **Shaoyan Liu:** Investigation, Data curation. **Jiabo Zhang:** Writing – review & editing, Project administration, Methodology, Conceptualization. **Zhen Huang:** Supervision, Resources. **Dong Han:** Writing – review & editing, Supervision, Resources, Project administration.

Declaration of competing interest

The authors declare that they have no known competing financial interests or personal relationships that could have appeared to influence the work reported in this paper.

Data availability

Data will be made available on request.

References

[1] Y. Jin, Z. Zheng, D. Wei, et al., Detection of micro-scale Li dendrite via H2 gas capture for early safety warning, Joule 4 (8) (2020) 1714–1729.

[2] J.A. Mennel, D. Chidambaram, A review on the development of electrolytes for lithium-based batteries for low temperature applications, Front. Energy 17 (1) (2023) 43–71.

[3] C.C. Chan, W. Han, H. Tian, et al., Automotive revolution and carbon neutrality, Front. Energy (2023), https://doi.org/10.1007/s11708-023-0890-8.

[4] C. Yang, X.-Y. Mu, Mapping the trends and prospects of battery cathode materials based on patent landscape, Front. Energy (2023), https://doi.org/10.1007/s11708-023-0900-x.

[5] K.C. Chiu, C.-H. Lin, S.-F. Yeh, et al., An electrochemical modeling of lithium-ion battery nail penetration, J. Power Sources 251 (2014) 254–263.

[6] G. Liang, Y. Zhang, Q. Han, et al., A novel 3D-layered electrochemical-thermal coupled model strategy for the nail-penetration process simulation, J. Power Sources 342 (2017) 836–845.

[7] S. Santhanagopalan, P. Ramadass, J. Zhang, Analysis of internal short-circuit in a lithium ion cell, J. Power Sources 194 (1) (2009) 550–557.

[8] B. Liu, Y. Jia, J. Li, et al., Safety issues caused by internal short circuits in lithium-ion batteries, J. Mater. Chem. A 6 (43) (2018) 21475–21484.

[9] J. Ye, H. Chen, Q. Wang, et al., Thermal behavior and failure mechanism of lithium ion cells during overcharge under adiabatic conditions, Appl. Energy 182 (2016) 464–474.

[10] D. Ren, X. Feng, L. Lu, et al., An electrochemical-thermal coupled overcharge-to-thermal-runaway model for lithium ion battery, J. Power Sources 364 (2017) 328–340.

[11] L. Huang, Z. Zhang, Z. Wang, et al., Thermal runaway behavior during overcharge for large-format Lithium-ion batteries with different packaging patterns, J. Energy Storage 25 (2019) 100811–100817.

[12] D. Ren, X. Feng, L. Lu, et al., Overcharge behaviors and failure mechanism of lithium-ion batteries under different test conditions, Appl. Energy 250 (2019) 323–332.

[13] Z. Wang, J. Yuan, X. Zhu, et al., Overcharge-to-thermal-runaway behavior and safety assessment of commercial lithium-ion cells with different cathode materials: a comparison study, J. Energy Chem. 55 (2021) 484–498.

[14] J. Liu, Z. Wang, J. Bai, et al., Heat generation and thermal runaway mechanisms induced by overcharging of aged lithium-ion battery, Appl. Therm. Eng. 212 (2022) 118565–118575.

[15] Z. Liu, X. Guo, N. Meng, et al., Study of thermal runaway and the combustion behavior of lithium-ion batteries overcharged with high current rates, Thermochim. Acta 715 (2022) 179276–179287.

[16] C. Jin, Y. Sun, H. Wang, et al., Model and experiments to investigate thermal runaway characterization of lithium-ion batteries induced by external heating method, J. Power Sources 504 (2021) 230065–230075.

[17] Q. Zhang, T. Liu, Q. Wang, Experimental study on the influence of different heating methods on thermal runaway of lithium-ion battery, J. Energy Storage 42 (2021) 103063–103071.

[18] Z. Zhou, X. Ju, X. Zhou, et al., A comprehensive study on the impact of heating position on thermal runaway of prismatic lithium-ion batteries, J. Power Sources 520 (2022) 230919–230929.

[19] X. Feng, M. Ouyang, X. Liu, et al., Thermal runaway mechanism of lithium ion battery for electric vehicles: a review, Energy Storage Mater. 10 (2018) 246–267.

[20] Q. Wang, B. Mao, S.I. Stoliarov, et al., A review of lithium ion battery failure mechanisms and fire prevention strategies, Prog. Energy Combust. Sci. 73 (2019) 95–131.

[21] P. Huang, C. Yao, B. Mao, et al., The critical characteristics and transition process of lithium-ion battery thermal runaway, Energy 213 (2020) 119082–119094.

[22] X. Feng, S. Zheng, D. Ren, et al., Investigating the thermal runaway mechanisms of lithium-ion batteries based on thermal analysis database, Appl. Energy 246 (2019) 53–64.

[23] B. Mao, P. Huang, H. Chen, et al., Self-heating reaction and thermal runaway criticality of the lithium ion battery, Int. J. Heat Mass Tran. 149 (2020) 119178–119186.

[24] X. Feng, M. Fang, X. He, et al., Thermal runaway features of large format prismatic lithium ion battery using extended volume accelerating rate calorimetry, J. Power Sources 255 (2014) 294–301.

[25] W. Xie, X. Liu, R. He, et al., Challenges and opportunities toward fast-charging of lithium-ion batteries, J. Energy Storage 32 (2020) 101837–101858.

[26] Q. Wang, X. Zhao, J. Ye, et al., Thermal response of lithium-ion battery during charging and discharging under adiabatic conditions, J. Therm. Anal. Calorim. 124 (1) (2016) 417–428.

[27] X. Feng, X. He, M. Ouyang, et al., A coupled electrochemical-thermal failure model for predicting the thermal runaway behavior of lithium-ion batteries, J. Electrochem. Soc. 165 (16) (2018) A3748–A3765.

[28] Z. An, K. Shah, L. Jia, et al., Modeling and analysis of thermal runaway in Li-ion cell, Appl. Therm. Eng. 160 (2019) 113960–113969.

[29] L.S. Guo, Z.R. Wang, J.H. Wang, et al., Effects of the environmental temperature and heat dissipation condition on the thermal runaway of lithium ion batteries during the charge-discharge process, J. Loss Prev. Process. Ind. 49 (2017) 953–960.

[30] J. Liu, Z. Wang, J. Gong, et al., Experimental study of thermal runaway process of 18650 lithium-ion battery, Materials 10 (3) (2017) 230–239.

[31] T. Gao, Z. Wang, S. Chen, et al., Hazardous characteristics of charge and discharge of lithium-ion batteries under adiabatic environment and hot environment, Int. J. Heat Mass Tran. 141 (2019) 419–431.

[32] J. Hu, T. Liu, X. Wang, et al., Investigation on thermal runaway of 18,650 lithium ion battery under thermal abuse coupled with charging, J. Energy Storage 51 (2022) 104482–104493.

[33] D. Meng, X. Wang, M. Chen, et al., Effects of environmental temperature on the thermal runaway of lithium-ion batteries during charging process, J. Loss Prev. Process. Ind. 83 (2023) 105084–105096.

[34] S. Koch, A. Fill, K.P. Birke, Comprehensive gas analysis on large scale automotive lithium-ion cells in thermal runaway, J. Power Sources 398 (2018) 106–112.

[35] Y. Zhang, H. Wang, W. Li, et al., Quantitative identification of emissions from abused prismatic Ni-rich lithium-ion batteries, eTransportation 2 (2019) 100031–100040.

[36] Z. Liao, S. Zhang, K. Li, et al., Hazard analysis of thermally abused lithium-ion batteries at different state of charges, J. Energy Storage 27 (2020) 101065–101073.

[37] J. Schmitt, B. Kraft, J.P. Schmidt, et al., Measurement of gas pressure inside large-format prismatic lithium-ion cells during operation and cycle aging, J. Power Sources 478 (2020) 228661–228670.

[38] P. Qin, J. Sun, Q. Wang, A new method to explore thermal and venting behavior of lithium-ion battery thermal runaway, J. Power Sources 486 (2021) 229357–229363.

[39] Z. Jia, P. Qin, Z. Li, et al., Analysis of gas release during the process of thermal runaway of lithium-ion batteries with three different cathode materials, J. Energy Storage 50 (2022) 104302–104313.

[40] B. Mao, H. Chen, L. Jiang, et al., Refined study on lithium ion battery combustion in open space and a combustion chamber, Process Saf. Environ. Protect. 139 (2020) 133–146.

[41] X. Feng, X. He, M. Ouyang, et al., Thermal runaway propagation model for designing a safer battery pack with 25 Ah LiNi Co Mn O2 large format lithium ion battery, Appl. Energy 154 (2015) 74–91.

[42] J. Zhang, A. Zhong, Z. Huang, et al., Experimental and kinetic study on the stabilities and gas generation of typical electrolyte solvent components under oxygen-lean oxidation and pyrolysis conditions, Sci. China Technol. Sci. 65 (12) (2022) 2883–2894.

[43] Q. Guo, J. Zhang, C. Zhou, et al., Thermal runaway behaviors and kinetics of NCM lithium-ion batteries at different heat dissipation conditions, J. Electrochem. Soc. 170 (8) (2023) 80507–80518.

[44] G. Liu, M. Ouyang, L. Lu, et al., Analysis of the heat generation of lithium-ion battery during charging and discharging considering different influencing factors, J. Therm. Anal. Calorim. 116 (2) (2014) 1001–1010.

[45] J. Zhang, Q. Guo, S. Liu, et al., Investigation on gas generation and corresponding explosion characteristics of lithium-ion batteries during thermal runaway at different charge states, J. Energy Storage 80 (2024) 110201–110211.

[46] B. Mao, C. Fear, H. Chen, et al., Experimental and modeling investigation on the gas generation dynamics of lithium-ion batteries during thermal runaway, eTransportation 15 (2023) 100212–100222.

[47] J.K. Ostanek, W. Li, P.P. Mukherjee, et al., Simulating onset and evolution of thermal runaway in Li-ion cells using a coupled thermal and venting model, Appl. Energy 268 (2020) 114972–114990.

[48] S. Hoelle, S. Scharner, S. Asanin, et al., Analysis on thermal runaway behavior of prismatic lithium-ion batteries with autoclave calorimetry, J. Electrochem. Soc. 168 (12) (2021) 120515–120525.

[49] P.T. Coman, S. Mátéfi-Tempfli, C.T. Veje, et al., Modeling vaporization, gas generation and venting in Li-ion battery cells with a dimethyl carbonate electrolyte, J. Electrochem. Soc. 164 (9) (2017) A1858–A1865.

[50] Y. Fernandes, A. Bry, S. De Persis, Identification and quantification of gases emitted during abuse tests by overcharge of a commercial Li-ion battery, J. Power Sources 389 (2018) 106–119.

[51] N. Sato, Thermal behavior analysis of lithium-ion batteries for electric and hybrid vehicles, J. Power Sources 99 (1) (2001) 70–77.

[52] K. Onda, H. Kameyama, T. Hanamoto, et al., Experimental study on heat generation behavior of small lithium-ion secondary batteries, J. Electrochem. Soc. 150 (2003) A285–A291.

[53] K. Onda, T. Ohshima, M. Nakayama, et al., Thermal behavior of small lithium-ion battery during rapid charge and discharge cycles, J. Power Sources 158 (1) (2006) 535–542.

[54] W. Shao, B. Zhao, W. Zhang, et al., Study on the reversible and irreversible heat generation of the lithium-ion battery with LiFePO4 cathode, Fire Technol. 59 (2) (2023) 289–303.

[55] D.J. Noelle, M. Wang, A.V. Le, et al., Internal resistance and polarization dynamics of lithium-ion batteries upon internal shorting, Appl. Energy 212 (2018) 796–808.

[56] W. Lu, J. Prakash, In situ measurements of heat generation in a Li/mesocarbon microbead half-cell, J. Electrochem. Soc. 150 (2003) A262–A266.

[57] D. Ouyang, M. Chen, J. Liu, et al., Investigation of a commercial lithium-ion battery under overcharge/over-discharge failure conditions, RSC Adv. 8 (58) (2018) 33414–33424.

[58] G. Zhang, X. Wei, J. Zhu, et al., Revealing the failure mechanisms of lithium-ion batteries during dynamic overcharge, J. Power Sources 543 (2022) 231867–231881.

[59] R. Leising, M. Palazzo, E. Takeuchi, et al., Abuse testing of lithium-ion batteries: characterization of the overcharge reaction of LiCoO2/graphite cells, J. Electrochem. Soc. 148 (2001) A838–A844.

[60] L. Liu, X. Feng, C. Rahe, et al., Internal short circuit evaluation and corresponding failure mode analysis for lithium-ion batteries, J. Energy Chem. 61 (2021) 269–280.

[61] M. Schmid, C. Endisch, Online diagnosis of soft internal short circuits in series-connected battery packs using modified kernel principal component analysis, J. Energy Storage 53 (2022) 104815–104829.

[62] L. Liao, X. Hu, H. Chen, et al., Quantitative diagnosis of micro-short circuit for lithium-ion batteries considering aging based on incremental capacity curve, J. Energy Storage 79 (2024) 110240–110254.

[63] G. Zhang, X. Wei, X. Tang, et al., Internal short circuit mechanisms, experimental approaches and detection methods of lithium-ion batteries for electric vehicles: a review, Renew. Sustain. Energy Rev. 141 (2021) 110790–110811.